



IUTAM_ABCM Symposium on Laminar Turbulent Transition

Numerical investigation of classical and bypass transition in streamwise corner-flow

Oliver T. Schmidt^a, Ulrich Rist^a

^a*Institut für Aerodynamik und Gasdynamik, Universität Stuttgart, Stuttgart, Germany*

Abstract

The laminar-turbulent transition of the flow in a zero-pressure-gradient streamwise corner is investigated by means of direct numerical simulation (DNS). Two basic scenarios are considered: transition caused by harmonic Tollmien-Schlichting type waves within the boundary-layer, and bypass transition triggered by homogeneous isotropic turbulence in the free-stream. In the first case, we further distinguish between waves that are symmetric, and waves that are anti-symmetric with respect to the corner bisector. It is found that turbulence originates from the corner in the classical boundary-layer transition scenario for both, symmetric and anti-symmetric perturbations. However, no such preference for the near-corner region is observed in bypass transition.

© 2014 The Authors. Published by Elsevier B.V.

Selection and peer-review under responsibility of ABCM (Brazilian Society of Mechanical Sciences and Engineering).

Keywords: Type your keywords here, separated by semicolons ;

1. Introduction

The laminar-turbulent transition of the flow along two semi-infinite perpendicular flat plates at zero angle of incidence is investigated numerically. In particular, we consider the transition upon the self-similar laminar base-state first calculated by Rubin & Grossman¹ for the incompressible and by Mikhail & Ghia² for general compressible fluids. In experiment, the laminar base-flow and its transition to turbulence was extensively studied in the 1970s and 1980s. The results of multiple experimental studies were summarised by Zamir³. Two main observations were consistently made: the experimental realisation of the flow deviates from the self-similar solution in form of an outward bulge in the lines of constant streamwise velocity in the near-corner region, and transition occurs much earlier than for the Blasius flat-plate scenario. Later, it was demonstrated by Kornilov & Kharitonov⁴ that the base-flow deviation from the theoretical solutions stems from the pressure gradient induced by the leading edge, also in experiment. Recently, Schmidt⁵ demonstrated that such a deformation has a drastic destabilising effect (in terms of linear stability) on the laminar flow. In the present study, the well-established self-similar state is investigated for comparability.

The scope of our work is to shed some light on the relevance of the different paths to transition for the corner-flow problem, i.e. Tollmien-Schlichting-wave induced transition and bypass transition under free-stream turbulence

E-mail address: o.schmidt@iag.uni-stuttgart.de

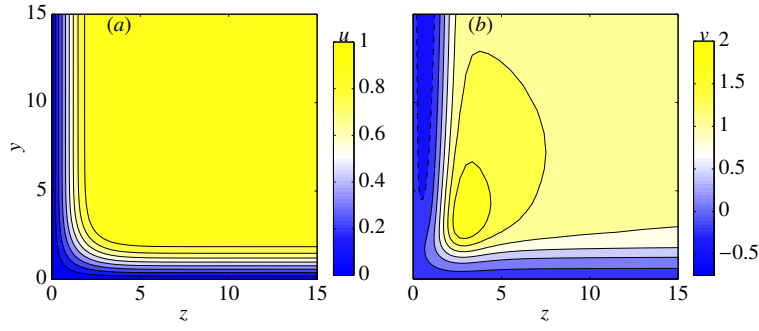


Fig. 1. Self-similar base-flow in the transverse plane⁷: (a) streamwise velocity; (b) lower wall-normal cross-flow velocity.

(FST). The numerical tools and the laminar base-state are reviewed in §2, results of the classical and bypass transition simulations are presented in §§3.1 and 3.2, respectively, and a discussion is given in §4.

2. Numerical methods and laminar base-state

The flow of a compressible Newtonian fluid is generally governed by the full Navier-Stokes equations

$$\frac{\partial \rho}{\partial t} = -\nabla \cdot \rho \mathbf{u}, \quad (1)$$

$$\frac{\partial \rho \mathbf{u}}{\partial t} = -\frac{1}{2} \nabla \cdot (\mathbf{u} \otimes \rho \mathbf{u} + \rho \mathbf{u} \otimes \mathbf{u}) - \nabla p + \frac{1}{Re} \nabla \cdot \boldsymbol{\tau}, \quad (2)$$

$$\frac{\partial \rho e}{\partial t} = -\nabla \cdot \rho e \mathbf{u} + \frac{1}{(\gamma - 1) Re Pr Ma_\infty^2} \nabla \cdot k \nabla T - \nabla \cdot p \mathbf{u} + \frac{1}{Re} \nabla \cdot \boldsymbol{\tau} \mathbf{u}, \quad (3)$$

where ρ is the density, $\mathbf{u} = (u, v, w)^T$ the velocity vector in the Cartesian coordinate frame $\mathbf{x} = (x, y, z)^T$, p the pressure, T the temperature and e the total energy. The dynamic viscosity μ and the thermal conductivity k are material properties. The pressure is non-dimensionalised by twice the dynamic pressure $\rho_\infty^* u_\infty^{*2}$, coordinates by the local displacement thickness $\delta_1^* = \int_0^\infty [1 - \rho^* u^* / \rho_\infty^* u_\infty^*] dy^*$ and all other quantities by their respective free-stream value. Superscript (*) and subscript (∞) denote dimensional quantities and free-stream values, respectively. The full Navier-Stokes equations (1-3) are solved by the direct numerical simulation (DNS) code NS3D⁶ for the simulation of three transition scenarios presented in §3. Sixth-order accurate compact finite differences are used for the spatial discretisation, and a standard fourth-order accurate Runge-Kutta method for integration in time. A Reynolds decomposition ansatz that separates a given flow quantity q into a steady base part q_0 and a fluctuation part q' allows us to enforce boundary conditions on the fluctuation part only, see e.g. Schmidt⁵. The steady laminar base-state as depicted in figure 1 is obtained as a solution to the parabolised Navier-Stokes equations⁸ and corresponds to the lower branch of the dual solution found by Ridha⁹. Along the two flat plates at some distance away from the intersection, the streamwise velocity as seen in figure 1a resembles the Blasius scenario. The complex cross-flow pattern visualised in figure 1b is a result of the superposition of the displacement effects of the adjacent walls. Its asymptotic behaviour is the main reason why we rely on a perturbation formulation for the DNS. The free-stream and material properties correspond to dry air at a Mach number of $Ma = 0.8$ and a temperature of $T_\infty = 300\text{K}$. In order to trigger classical (Tollmien-Schlichting-wave induced) transition (§3.1), periodic wall heating and cooling is applied in a narrow band close to the inlet of the computational box in order to force harmonic oscillations with an initial amplitude of $|u'| \approx 6\%$. A perturbation frequency of $\omega = 0.09$ is chosen to guarantee high spatial amplification. In §3.2, isotropic and homogeneous FST enters through the inlet and triggers bypass transition. It is generated as a superposition of continuous mode solutions to the underlying linear stability problem following the ansatz by Jacobs & Durbin¹⁰. For the present study, the method is extended to compressible flows and two-dimensional eigenfunctions. The linear stability eigenvalue problem in the transverse plane is set up and solved as described in Schmidt & Rist⁸, except for the spatial discretisation. Here, fifth-order accurate finite differences upon a uniform grid are used instead of a spectral approach

to calculate continuous mode solutions. In order to be realistic, the artificial inflow turbulence is desired to have the wave number distribution corresponding to the empirical von Kármán spectrum

$$E_{ref}(k) = \frac{2}{3} \frac{a(kL)^4}{(b + (kL)^2)^{17/6}} Lq, \quad (4)$$

i.e. apart from being isotropic and homogeneous. Here, k is the modulus of the wavenumber vector $\mathbf{k} = (k_x, k_y, k_z)^T$, $a = 1.606$ and $b = 1.350$ are empirical constants, $L = 2.5$ the turbulence integral length scale chosen for the current investigation, and $q = \int E(k) dk = \frac{1}{2} \overline{\mathbf{u}' \cdot \mathbf{u}'}$ the turbulence kinetic energy. The spectral content of each individual continuous mode in terms of k_y and k_z is obtained via a two-dimensional Fourier decomposition of the corresponding eigenfunction, whereas the streamwise wave number k_x is a free parameter of the linear stability problem. Note that this step is not necessary in the case where the spanwise direction is homogeneous and the wall-normal wave number can be fixed by an appropriate boundary condition, e.g. as for the flat plate. Here, however, k_y and k_z are intrinsic to the eigenfunctions. A basis consisting of 2500 modes was found sufficient to meet the requirements posed on the above turbulence properties. The allowed streamwise wave number space was uniformly divided into 50 intervals of k_x , and 600 continuous modes were calculated for each k_x using the standard shift-invert Arnoldi method, out of which 50 were randomly chosen to form the basis. Before that, unsuitable modes were filtered out, i.e. entropy and pressure waves. The minimum and maximum wavenumbers are determined by the spanwise computational domain extent and the maximum grid spacing through the Nyquist criterion, respectively, and dictate the allowed wavenumber regime, i.e. $0.136 \leq k_x, k_y, k_z \leq 2.001$. For the sake of homogeneity, the same limits are applied in all directions. In the homogeneous case, e.g. in the work of Jacobs & Durbin¹⁰ or Brandt et al.¹¹, modes are calculated for specific values k_x , k_y and k_z . Hence, the modal wave number magnitude is set/known and the modal amplitudes are chosen such that the desired spectrum is met. The non-homogeneous two-dimensional eigenfunctions at hand, however, feature a banded wavenumber distribution in the spanwise directions. In other words, an individual mode cannot be associated with just one specific wave number modulus. In order to find the modal amplitudes A_m such that the modal superposition (sum in equation 5) results in the target spectrum $E_{ref}(k)$, we formulate an optimisation problem of the form

$$\min_{|A_m|, k_i \leq k_i \leq k_u} \left\| \left(\sum_{m=1}^m A_m^2 E_{\mathbf{u}\mathbf{u},m}^{(i)} \right) - E_{ref}^{(i)} \right\|_2^2 \quad (5)$$

to find an approximative solution in a least-squares sense. Note that the unknown model parameters A_m appear squared as the reference function is of energy-type. We apply a standard iterative Levenberg-Marquardt algorithm to solve the above non-linear least squares problem. The so-modelled FST is found homogeneous and isotropic after a short initial transient of $\approx 5\%$ of the computational box length, where the streamwise perturbation velocity lags behind the spanwise components. However, this initial stage is not of interest as the main receptivity process takes place some distance further downstream as discussed later in §3.2.

The computational box sizes and resolutions for the DNS are listed in table 1 below. At the outlet, a sponge region with a spatial extent of 2% of the domain length that forces all perturbations to zero is combined with a subsonic outflow condition¹² in all simulations. Walls are being assumed to be adiabatic. Homogeneous Neumann conditions are enforced on the far-field boundaries, with and without sponge for the bypass and classical transition calculations, respectively, as well as on the inlet for the classical transition cases. Note that the Neumann conditions are compatible with the forced two-dimensional waves in the classical scenario simulations. The artificial FST is directly prescribed at the inlet in form of a non-homogeneous Dirichlet condition.

Table 1. Computational domains; $Re_{x,0}$ and $Re_{x,1}$ are the local Reynolds numbers at the beginning and the end of the computational box, respectively. $x_{p,0}$ and $x_{p,1}$ denote the beginning and the end of the wall-forcing strip, Tu is the turbulence intensity, y_1 and z_1 are the domain extents in the spanwise directions, N denotes the number of grid points in the respective direction (subscript), and Δt the numerical time step.

case	$Re_{x,0}$	$Re_{x,1}$	$x_{p,0}$	$x_{p,1}$	Tu [%]	y_1	z_1	N_x	N_y	N_z	Δt
<i>wall-forcing</i>	15×10^4	42.5×10^4	197.12	208.61	-	54	54	1250	400	400	0.005
<i>free-stream turbulence</i>	15×10^4	70×10^4	-	-	3	54	25	2500	214	400	0.005

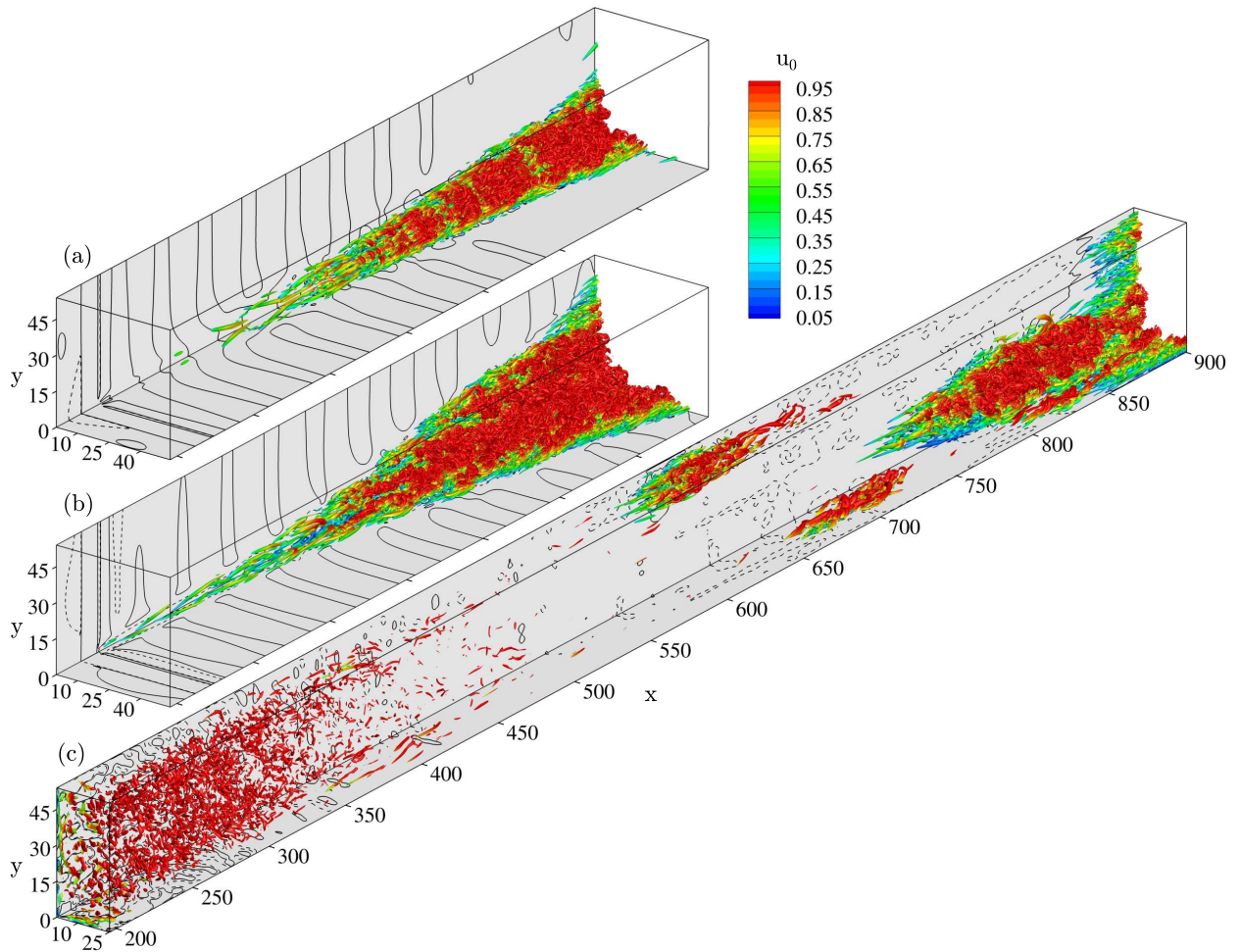


Fig. 2. Instantaneous visualization of the transition process; isosurfaces of the λ_2 -criterion at $\lambda_2 = -0.01$ coloured by the local streamwise velocity of the base-state, and isocontours of the wall pressure perturbation at $\rho' = 0.002$ (—) and $\rho' = -0.002$ (---): (a) symmetric wall forcing, (b) anti-symmetric wall forcing, (c) FST.

3. Results

All results presented in the following are obtained after all initial transients have decayed, i.e. for times longer than about two flow-through times. An overview of all three calculations at a representative time instant is shown in figure 2. Here, transitional or turbulent parts of the flow are accentuated by means of coloured λ_2 -isosurfaces. The qualitative difference between the routes to transition for the wall-forced cases in figure 2a-b, and the FST case in figure 2c is apparent at first glance: turbulence develops in form of a wedge along the corner in both cases of periodic wall forcing, whereas seemingly randomly located turbulent spots emerge under FST. The two scenarios are analysed in detail in the following.

3.1. Classical transition

From figure 2a-b, it is observed that the corner region plays a decisive role in the onset of turbulence under periodic forcing, and that turbulence spreads at a larger angle under anti-symmetric forcing. A likely cause for the latter observation is the perturbation shear stress induced by the phase-shift between the lower- and back-wall forcing.

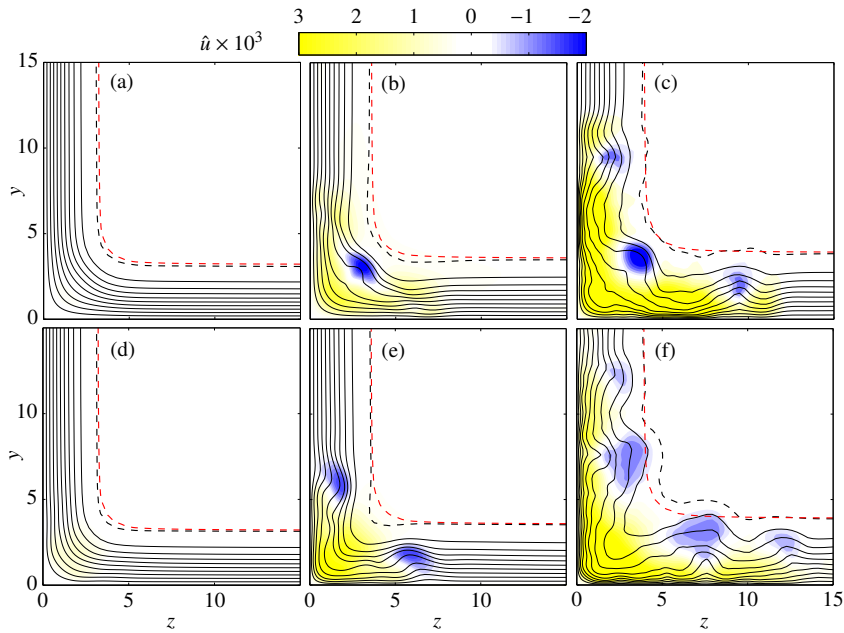


Fig. 3. Isocontours of the time-averaged streamwise velocity \bar{u} (—, in 10% increments), and mean-flow deformation in transversal planes for symmetric (a-b) and anti-symmetric (d-f) forcing: (---) δ_{99} of \bar{u} ; (- - -) δ_{99} of u_0 : (a,d) $x = 267.49$, (b,e) $x = 332.12$, and (c,f) $x = 396.74$, corresponding to the beginning, the middle, and the end of the DMD subdomain, respectively.

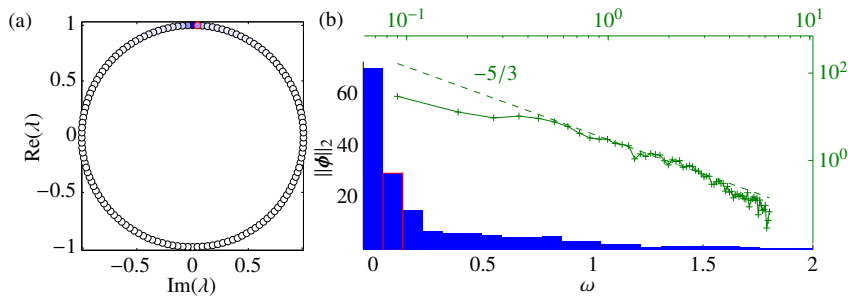


Fig. 4. Dynamic mode decomposition of the symmetric forcing data from 140 snapshots over one fundamental period: (a) empirical Ritz values (○); (b) magnitudes of the Koopman modes on a linear (■, lower left) and a logarithmic scale (—, upper right). The dashed line (---) shows a slope of $\omega^{-5/3}$, and the forcing frequency is highlighted by (○) and (□) in (a) and (b), respectively.

The time-averaged streamwise velocity $\bar{u} = N^{-1} \sum_{i=1}^N u_i$ and mean-flow deformation $\bar{u}' = \bar{u} - u_0$ fields at three streamwise locations within the early stage of transition are shown in figure 3. The average is taken over one fundamental forcing period. The top and bottom row depict the symmetric and anti-symmetric case, respectively. At a position closely behind the perturbation strip as seen in figures 3a and 3d, no significant deviation from the laminar state is observed. A position further downstream, non-linear interactions lead to a mean-flow distortion in form of a convex bulge in the corner region in the symmetric case. In the anti-symmetric case, a concave deformation is observed which is flanked by outward bulges at the edges of the turbulent wedge on both sides. Even further downstream, both cases show a significant deformation from the self-similar base-state. All deformations described above lead to highly inflectional streamwise mean velocity profiles that are prone to secondary instability. Therefore, rapid transition and the observed spanwise spread of turbulence is not unexpected.

The transitional flow is decomposed using the DMD method by Schmid¹³ using a 140 snapshot basis, uniformly distributed over one fundamental period. The spectral analysis is conducted within a $[267.5, 396.7] \times [0, 22.8] \times [0, 22.8]$ subdomain that covers the initial stage of transition behind the perturbation source. The empirical Ritz values are depicted in figure 4a in the complex plane. It can be seen that all Ritz values are located on the unit circle,

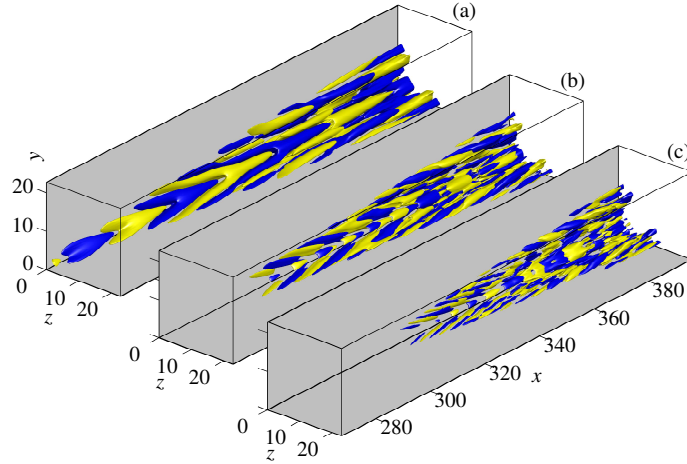


Fig. 5. Dynamic modes of the transitional DNS visualized by isosurfaces of the streamwise perturbation velocity; (■) $\hat{u} = 0.2|\hat{u}|_{max}$, (■) $\hat{u} = -0.2|\hat{u}|_{max}$: (a) fundamental frequency $\text{Im}(\omega) = 0.09$, (b) first higher harmonic $\text{Im}(\omega) = 0.18$, and (c), second higher harmonic $\text{Im}(\omega) = 0.27$.

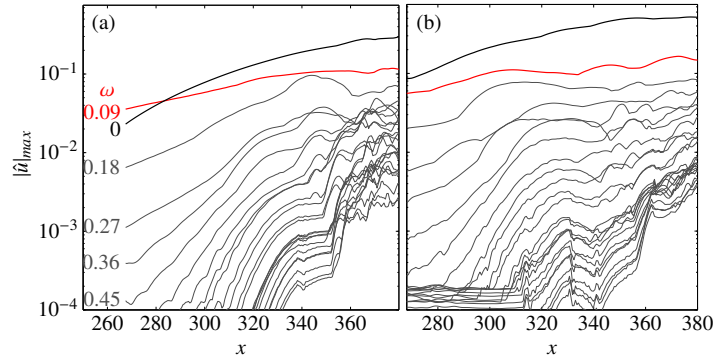


Fig. 6. Downstream development of DMD modes in terms of the local maximum of the streamwise perturbation velocity: (—) forcing frequency; (—) mean-flow deformation; (—) higher harmonics.

indicating zero temporal growth as expected for a convective problem on its limit cycle. Also, the values are evenly distributed, meaning that the flow field is clearly decomposed into mono-frequency modes of integer multiples of the forcing frequency. The modal amplitudes are shown in figure 4b as a function of the modal frequency on a linear and a logarithmic scale in the same plot. The first Koopman mode is found to be the most energetic. This result is not surprising as the first mode embodies the steady component with $\omega = 0$ which is similar but not necessarily equal to the mean-flow deformation¹⁴. The second most energetic mode is the direct response of the base-state to the forcing frequency at $\omega = 0.09$. For higher frequencies, the modal energy distribution is found in good agreement with the $-5/3$ power-law of the inertial subrange of the energy cascade.

The modal structures corresponding to the fundamental frequency and the first two higher harmonics are visualized in figure 5 for the symmetric case. It can be seen that energy is distributed towards higher wave numbers in accordance with the energy cascade. This is clearly indicated by the increasingly fine flow patterns when comparing the modes in the given order of increasing frequency. The same holds for the anti-symmetric case (not depicted here).

The spatial perturbation development by means of the modal local maximum of the streamwise perturbation velocity is examined in figure 6 by means of the local velocity maximum at each streamwise location. It can be seen that the mean-flow deformation gains approximately one order of magnitude while almost monotonically increasing its amplitude from $\approx 2\%$ at the beginning to $\approx 30\%$ of the free-stream velocity at the end of the DMD subdomain. The mode corresponding to the forcing frequency attains an amplitude of $\approx 12\%$. The higher frequency modes appear ordered by amplitude up to the fourth higher harmonic, and reach a level of saturation for $x \gtrsim 360$.

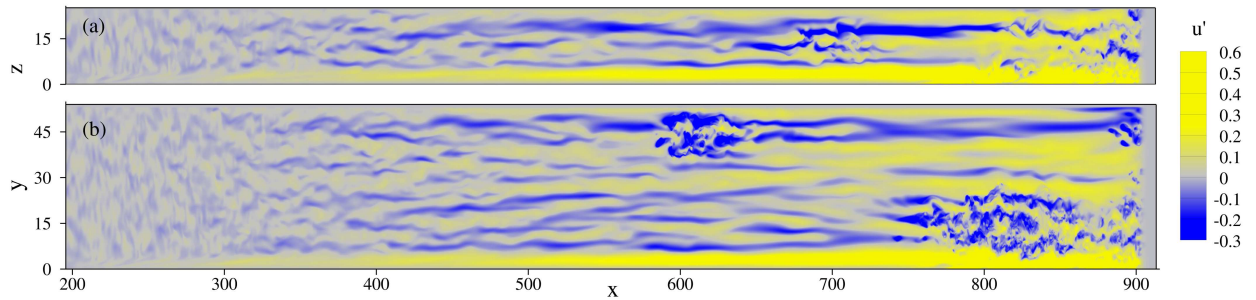


Fig. 7. Instantaneous visualization of the transition process under FST in terms of the streamwise perturbation velocity u' in wall-parallel planes: (a) $y = 3$, (b) $z = 3$. Note that the streamwise and spanwise coordinates are scaled differently.

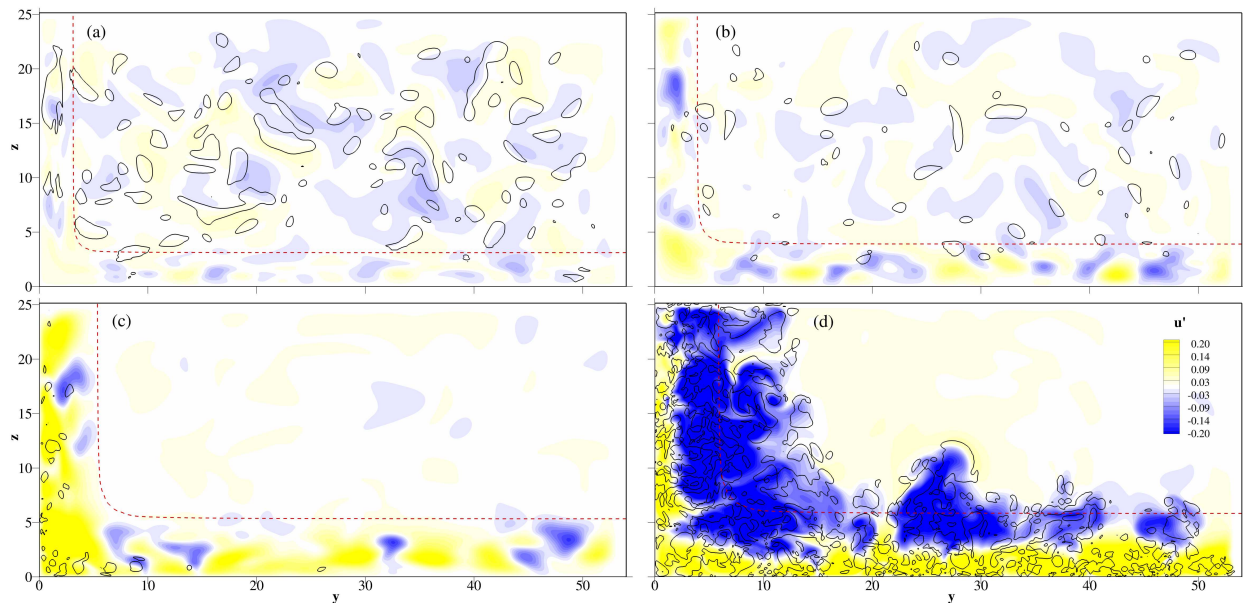


Fig. 8. Downstream development of the streamwise perturbation velocity and λ_2 under FST in transverse planes; (—) λ_2 ; (- - -) δ_{99} of the base-state: (a) $x = 253$, (b) $x = 396$, (c) $x = 741$, (d) $x = 884$.

3.2. Bypass transition

A decomposition as shown above is not feasible for the analysis of the bypass transition scenario as the transient data is neither periodic nor statistically converged. Hence we rely on a qualitative description of flow phenomena from instantaneous visualizations.

The visualization of the instantaneous streamwise perturbation velocity in wall-parallel planes within the boundary-layer in figure 7 reveals the typical characteristics of bypass transition: small-scale vortical disturbances penetrate the edge of the boundary layer and trigger the emergence of streamwise streaks through the lift-up effect¹⁵. Further downstream, streak instability gives birth to turbulent spots that grow in size and finally merge with others while being advected. Interestingly, a sustaining high-speed streak is observed right in the corner.

The different stages of receptivity and bypass transition can be seen in the transverse plane plots of the perturbation field in figure 8. Here, the streamwise perturbation velocity is shown alongside with the λ_2 -criterion to distinguish between streaks and vortical disturbances, respectively. In the beginning of the domain in figure 8a, vortical disturbances in the far-field are the dominant perturbation flow feature. In figure 8b at a position somewhat more downstream, streamwise streaks evolve within the boundary-layer while the far-field turbulence exponentially decays until becoming almost non-existent in 8c. In accordance with theory, the width of the streaks in 8b-c is found in the order

of the boundary-layer thickness. The above-mentioned high-speed streak can, again, be seen in the same plots. Close to the outlet in figure 8d, the boundary-layer flow is entirely transitional or turbulent. The typical turbulent exchange of momentum between the wall-near sublayer and the outer regions can be seen from the clear separation of high and low-speed perturbation velocity.

4. Conclusions

An interesting observation is the formation of a turbulent wedge originating from the corner under harmonic boundary-layer forcing. This is found in contrast to linear stability analyses as in the work of Parker & Balachandar¹⁶ or by the present authors⁸, which do not predict a reduced stability limit as compared to the Blasius flat plate flow. The latter represents the asymptotic solution for the streamwise and wall normal velocity components far away from the corner. A possible explanation for the preferred onset of instability in the near-corner region can be found in the sensitivity study by Alizard et al.¹⁷, and the linear stability analysis of a deformed base-flow by Schmidt⁵. The first mentioned authors demonstrated that the corner region is highly sensitive to base-flow modifications within a linear framework, and that a significant decrease in the critical Reynolds number can be expected due to such a modification. The second mentioned finds a drastic decrease of the linear instability limit for a deformed base-flow that mimics the outward bulge seen in experiment or as seen in this study in the mean field under symmetric forcing, compare figure 3b. Transient growth is another potential candidate to explain the observed behaviour. The linear non-modal analysis by Alizard et al.¹⁸ showed that temporal transient growth has to be expected. More recently, the present authors⁷ used the same framework as for this study to demonstrate that spatial transient growth indeed does occur in fully non-parallel simulations under periodic mono-frequency forcing at low amplitudes. The mechanism was analysed in detail using an eigenvector-expansion-based optimal perturbation technique. However, the amplification rates were found moderate and no significant spatial transient growth was observed in the present high-amplitude simulations.

From the numerical side, it was demonstrated that the construction of FST is feasible for non-homogeneous problems in which the eigenvectors are two-dimensional. The complication arising from the multiple wavenumber content of the basis vectors was solved by formulating a non-linear optimisation problem for the expansion coefficients. It has to be noted that our approach neglects certain potentially important non-parallel effects¹⁹, a property our results share with comparable flat plate studies such as the ones summarized by Durbin & Wu²⁰ that also use a continuous-mode-expansion method to construct artificial FST.

In summary, our results bring to light a fundamental difference between the two transition scenarios in streamwise corner-flow: in the case of harmonic forcing (both, symmetric and anti-symmetric), the corner itself plays a dominant role in the development of turbulence, while no such effect can be seen in the bypass scenario triggered by high turbulence level free-stream contamination.

References

1. Rubin, S.G., Grossman, B.. Viscous flow along a corner: numerical solution of the corner layer equations. *Quarterly of Applied Mathematics* 1971;**29**:169–186.
2. Mikhail, A.G., Ghia, K.N.. Viscous compressible flow in the boundary region of an axial corner. *AIAA Journal* 1978;**16**:931–939. doi:10.2514/3.60987.
3. Zamir, M.. Similarity and stability of the laminar boundary layer in a streamwise corner. *Royal Society of London Proceedings Series A* 1981;**377**:269–288.
4. Kornilov, V.I., Kharitonov, A.M.. On the part played by the local pressure gradient in forming the flow in a corner. *Fluid Dynamics* 1982; **17**:242–246. doi:10.1007/BF01314499.
5. Schmidt, O.T.. *Numerical investigations of instability and transition in streamwise corner-flows*. Ph.D. thesis; University of Stuttgart; 2014.
6. Babucke, A., Kloker, M.J., Rist, U.. DNS of a plane mixing layer for the investigation of sound generation mechanisms. *Computers & Fluids* 2008;**37**(4):360–368.
7. Schmidt, O.T., Rist, U.. Viscid–inviscid pseudo-resonance in streamwise corner flow. *Journal of Fluid Mechanics* 2014;**743**:327–357.
8. Schmidt, O.T., Rist, U.. Linear stability of compressible flow in a streamwise corner. *Journal of Fluid Mechanics* 2011;**688**:569–590.
9. Ridha, A.. On the dual solutions associated with boundary-layer equations in a corner. *Journal of Engineering and Mathematics* 1992; **26**:525–537.
10. Jacobs, R.G., Durbin, P.A.. Simulations of bypass transition. *Journal of Fluid Mechanics* 2001;**428**(-1):185–212.
11. Brandt, L., Schlatter, P., Henningson, D.S.. Transition in boundary layers subject to free-stream turbulence. *Journal of Fluid Mechanics* 2004;**517**(-1):167–198.

12. Babucke, A.. *Direct Numerical Simulation of Noise-Generation Mechanisms in the Mixing Layer of a Jet*. Ph.D. thesis; Universität Stuttgart; 2009.
13. Schmid, P.J.. Dynamic mode decomposition of numerical and experimental data. *Journal of Fluid Mechanics* 2010;**656**:5–28. doi:10.1017/S0022112010001217.
14. Chen, K.K., Tu, J.H., Rowley, C.W.. Variants of dynamic mode decomposition: boundary condition, Koopman, and Fourier analyses. *Journal of Nonlinear Science* 2011;:1–29.
15. Landahl, M.T.. A note on an algebraic instability of inviscid parallel shear flows. *Journal of Fluid Mechanics* 1980;**98**(02):243–251.
16. Parker, S.J., Balachandar, S.. Viscous and inviscid instabilities of flow along a streamwise corner. *Theoretical and Computational Fluid Dynamics* 1999;**13**:231–270. doi:10.1007/s001620050117.
17. Alizard, F., Robinet, J.C., Rist, U.. Sensitivity analysis of a streamwise corner flow. *Physics of Fluids* 2010;**22**(1):014103. doi:10.1063/1.3292009.
18. Alizard, F., Robinet, J.C., Guiho, F.. Transient growth in a right-angled streamwise corner. *European Journal of Mechanics-B/Fluids* 2012; **37**:99–111.
19. Dong, M., Wu, X.. On continuous spectra of the orr–sommerfeld/squire equations and entrainment of free-stream vortical disturbances. *Journal of Fluid Mechanics* 2013;**732**:616–659.
20. Durbin, P., Wu, X.. Transition beneath vortical disturbances. *Annu Rev Fluid Mech* 2007;**39**:107–128.